Supporting Information

Competition of Secondary versus Tertiary Carbenium Routes for the Type B Isomerization of Alkenes over Acid Zeolites Quantified by AIMD Simulations

Jérôme Rey,[1] Pascal Raybaud,[1] Céline Chizallet,[1,] Tomáš Bučko,[2,3,*]*

[1] IFP Energies nouvelles – Rond-Point de l'Echangeur de Solaize – BP 3 69360 Solaize, France

[2] Department of Physical and Theoretical Chemistry, Faculty of Natural Sciences, Comenius University in Bratislava, Ilkovičova 6, SK- 84215 Bratislava, Slovakia

[3] Institute of Inorganic Chemistry, Slovak Academy of Sciences, Dúbravská cesta 9, SK-84236 Bratislava, Slovakia

celine.chizallet@ifpen.fr; tomas.bucko@uniba.sk

SI. Supercell of chabazite

A primitive rhombohedral cell of purely siliceous chabazite (CHA framework, symmetry group R $\overline{3}$ m), with 12 symmetry equivalent tetrahedral sites, was obtained from International Zeolite Association (IZA) database.[1] The cell was reoptimized yielding the lattice constants a = 9.336 Å and α = 94.6°, which are in good agreement with the reference values[1] (a = 9.304 Å and α = 94.6°). The relaxed structure was subsequently used to build a supercell defined by lattice vectors $\mathbf{a}_1'$, $\mathbf{a}_2'$, and $\mathbf{a}_3'$ related to the primitive cell vectors of rhombohedral lattice ($\mathbf{a}_1, \mathbf{a}_2, \mathbf{a}_3$) via the following transformations: $\mathbf{a}_1' = \mathbf{a}_2 + \mathbf{a}_3$, $\mathbf{a}_2' = \mathbf{a}_1 + \mathbf{a}_3$, and $\mathbf{a}_3' = \mathbf{a}_1 + \mathbf{a}_2$. The shortest interatomic separation between the atoms in hydrocarbon and atoms in its periodically repeated images in the supercell was at least 5.5 Å. The Brønsted acid site was created by replacing one Si atom by an Al atom and inserting the H atom onto the framework oxygen atom O1 (Figure 2 in the main text), which is, according to experiment,[2] one of the two most populated proton sittings in CHA. In the gas phase simulations, the same unit cell as in the periodic calculations has been used.

SII. Rotational isomers of the species involved in both mechanisms

In subsection SII.1, we describe the rotational isomers for the cation I_1 in gas phase (as discussed in Section 3.1.a of the main text). In subsection SII.2, we provide the free energy profile for the torsion of the reactant R. In subsections SII.3 and SII.4, we provide the free energy profiles along the torsion coordinate τ defined below for the intermediate cation I_2 and the product I_3 in the gas phase and in chabazite. The relevant rotational isomers are identified, and their likelihoods of occurrence are computed.

SII.1. Cation I_1

Two stable rotamers I_1(I) and I_1(II) have been identified in gas phase (Figure S1). We note that the valence angle ($C^2C^3C^4$) is relatively sharp in both structures (96° in I_1(I) and 82° in I_1(II) and this structural preorganization also determines the isomerization mechanism via which these cations can transform.

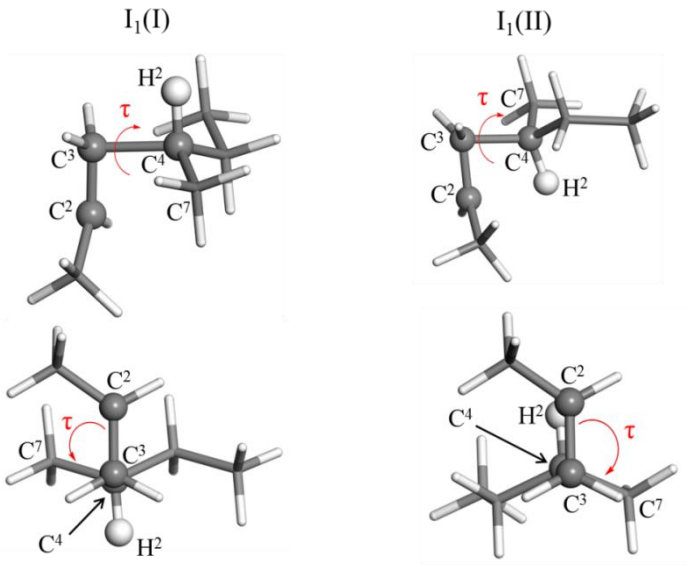

Figure S1. Rotational isomers $I_1(I)$ ($\tau \approx -71°$) and $I_1(II)$ ($\tau \approx 114°$) of the cation 4-methyl-hexen-2-ium. Top panels: side view; bottom panels: front view chosen so that the atom C^3 overlaps the atom C^4.

SII.2. Reactant R in chabazite

A constrained blue moon simulation has been carried out for the reactant molecule in CHA to study the free energy as a function of the dihedral angle (τ) between atoms C^2-C^3-C^4-C^7 (Figure 3) for T = 300 K and 500 K. The computed free energy profiles are presented Figure S2.

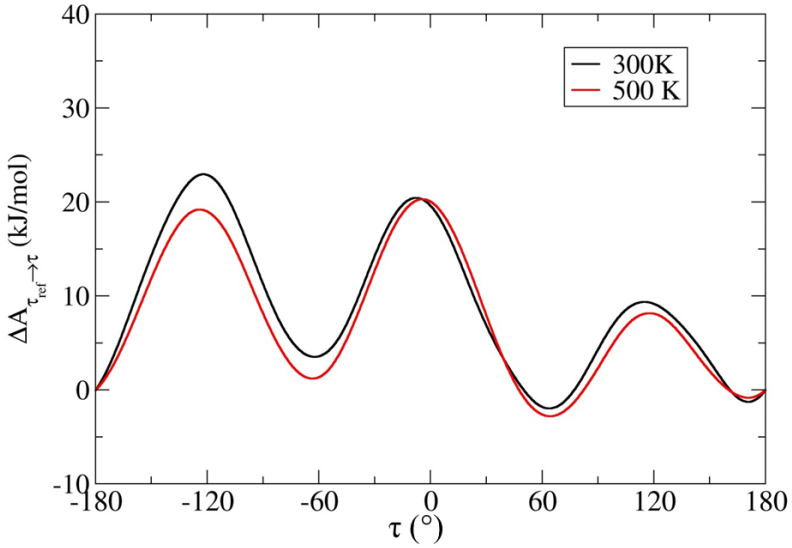

Figure S2. Free energy profile as a function of the torsion angle τ for the neutral molecule (R) in chabazite at T = 300 K and 500 K. Note that periodic boundary conditions apply, i.e. the point $\tau = -180°$ is identical to the point $\tau = 180°$.

SII.3. Intermediate I_2

The changes in geometry of the intermediate I_2 related to steps 1 and 2 of mechanism II can be controlled via the dihedral angle (τ) between the atoms C^1, C^2, C^3 and C^4 (Figure S3). The potential energy as a function of τ (Figure S4(a)) has been determined for the cation in the gas phase in a series of constrained relaxations. The corresponding free energy profiles and likelihoods of occurrence of individual rotamers among all I_2 states in chabazite (Figure S4(b)) have been determined by blue moon sampling in the same procedure as described in Section 3.1 for the R state.

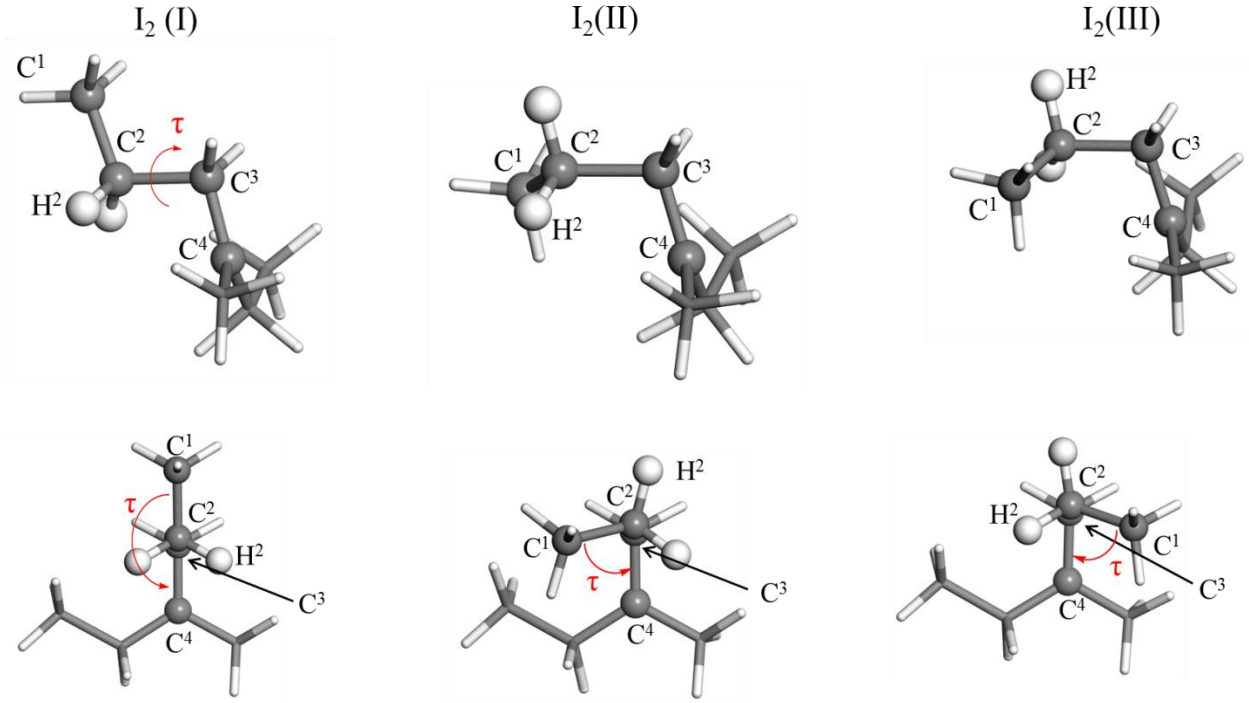

Figure S3. Rotational isomers I_2(I) (τ ≈ –180°), I2(II) (τ ≈ –69°), and I_2(III) (τ≈ 69°) of the product 2,3-dimethyl-penten-3-ium. Top panels: side view; bottom panels: front view chosen so that the atom C^2 overlaps the atom C^3.

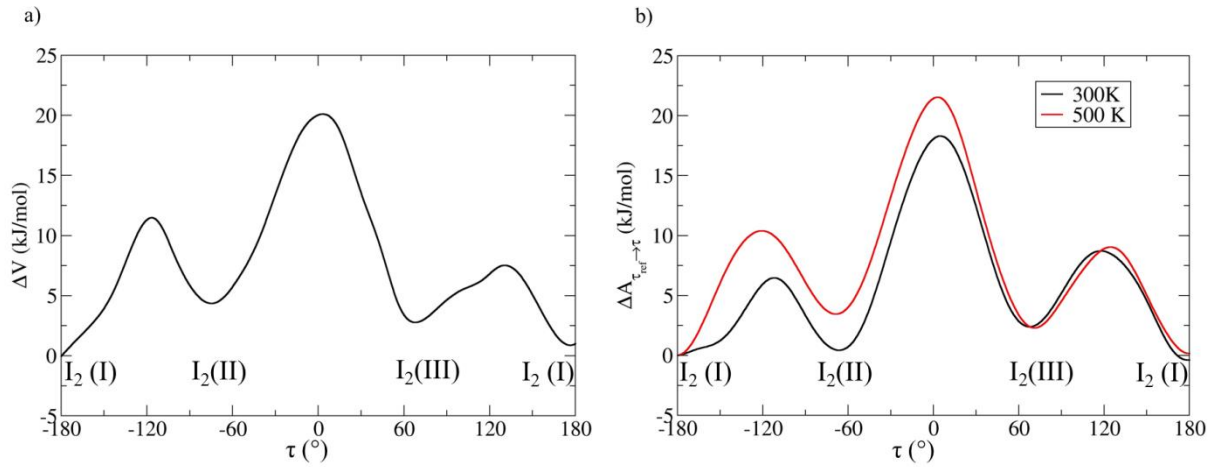

Figure S4. a) Potential energy as a function of dihedral angle (τ) defined by the atoms C^1, C^2, C^3 and C^4 (see Figure S3) computed using constrained relaxations of the cation (I_2) in the gas phase. Zero on the energy axis is defined by the energy of the lowest energy state. b) Free energy profile as a function of τ for the same cation I_2 located in chabazite at T = 300 K and 500 K. Note that periodic boundary conditions apply, i.e. the point $\tau = -180°$ is identical to the point $\tau = 180°$.

The numerical likelihoods of occurrence are compiled in Table S1.

Table S1. Likelihoods (%) of occurrence of individual rotamers of I_2 at 300 and 500 K.

	300 K	500 K
p(I_2(I))	56.5	49.7
p(I_2(II))	30.1	21.8
p(I_2(III))	13.4	28.5

SII.4. Product I_3

For the I_3 product, the changes in geometry related to mechanisms I and II can be controlled via the dihedral angle (τ) between the atoms C^3, C^2, C^4, and C^7 (Figure S5). The free energy profiles and likelihoods of occurrence of individual rotamers of I_2 among all states in chabazite (Figure S6) have been obtained in the same way as for the state R described in Section 3.1.

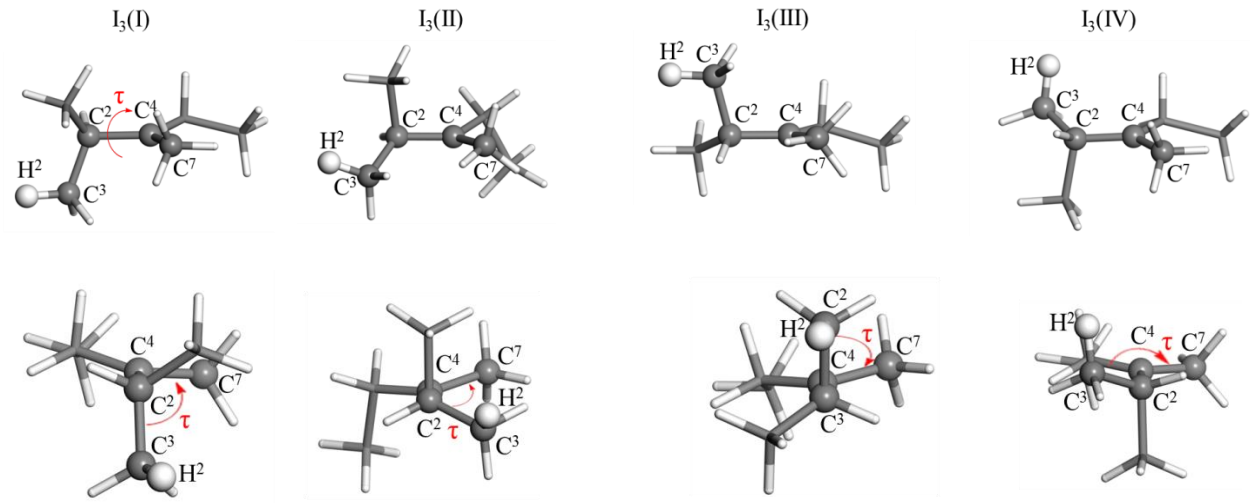

Figure S5. Rotational isomers I_3(I) ($\tau \approx -90°$), I_3(II) ($\tau \approx -30°$), I_3(III) ($\tau \approx 90°$) and I_3(IV) ($\tau \approx 150°$) of the 2,3-dimethyl-penten-3-ium cation I_3. Top panels: side view; bottom panels: front view chosen so that the atom C^2 overlaps the atom C^3.

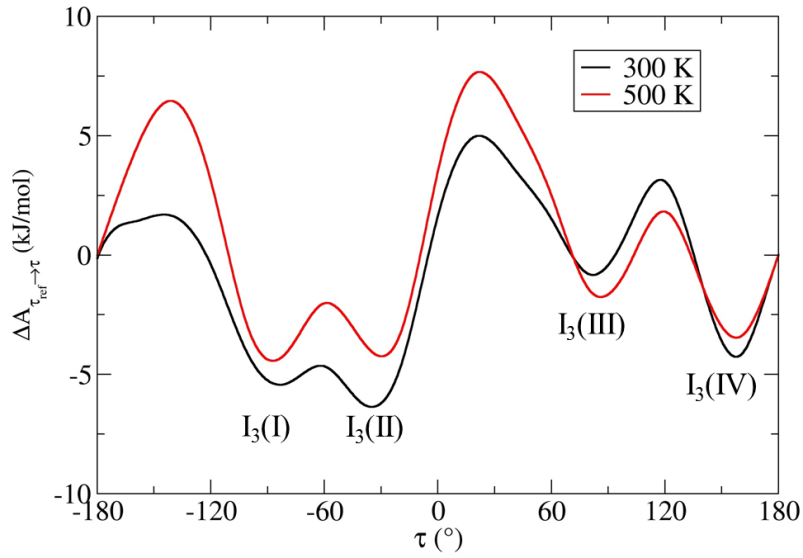

Figure S6. Free energy profiles as functions of the dihedral angle (τ) defined by the atoms C^3, C^2, C^4, and C^7 (Figure S3) for the product I_3 in chabazite at T = 300 K and 500 K. Note that periodic boundary conditions apply, i.e. the point $\tau = -180°$ is identical to the point $\tau = 180°$.

The likelihoods of occurrence are given in Table S2.

Table S2. Likelihoods (%) of occurrence of individual rotamers of I_3 at 300 and 500 K.

	300 K	500 K
p(I_3(I))	35.0	29.1
p(I_3(II))	44.5	27.8
p(I_3(III))	5.6	17.3
p(I_3(IV))	14.9	25.8

SIII. Determination of the velocity term $|\dot{\xi}^*|$

The term $\langle|\dot{\xi}^*|\rangle$) required in the calculations of free energy of activation (see Equation 1 in the main text) is determined using the constrained MD simulations via the formula:[3,4]

$$\langle|\dot{\xi}^*|\rangle = \sqrt{\frac{k_B T}{2\pi}} \frac{1}{\left\langle Z^{-1/2} \right\rangle_{\xi^*}}, \qquad \text{(Eq. S1)}$$

where the term enclosed in $\langle ... \rangle_{\xi^*}$ is computed as a statistical average for a constrained ensemble with $\xi(\boldsymbol{r}) = \xi^*$, and Z is the inverse of the mass metric tensor:

$$Z = \sum_{i=1}^{N} \frac{1}{m_i} \sum_{\mu=x,y,z} \left(\frac{\partial \xi}{\partial r_{i,\mu}} \right)^2, \qquad \text{(Eq. S2)}$$

with $r_{i,\mu}$ being the Cartesian component μ of the position vector of an atom i and the sums are over all atoms and Cartesian components. We note that the term $\left\langle Z^{-1/2} \right\rangle_{\xi^*}$ is readily available from the constrained MD performed for the state ξ^* within the $\Delta A_{\xi_{ref,X} \to \xi^*}$ calculation. The values of $\langle|\dot{\xi}^*|\rangle$ are compiled in Table S3.

Table S3. Average velocity $\langle|\dot{\xi}^*|\rangle$ (in s^{-1}) of reaction coordinate at the different transition states.

	Mechanism I	
	T (K)	$\langle\|\dot{\xi}^*\|\rangle$ (s^{-1})
TS(I)	300	$1.10 \cdot 10^{13}$
	500	$1.40 \cdot 10^{13}$

	Mechanism II	
	T (K)	$\langle\|\dot{\xi}^*\|\rangle$ (s^{-1})
TS(IIa)	300	$1.08 \cdot 10^{13}$
	500	$1.45 \cdot 10^{13}$
TS(IIb)	300	$9.90 \cdot 10^{12}$
	500	$1.26 \cdot 10^{13}$

SIV. Probability distribution functions $\widetilde{P}(\xi)$ for reactant, intermediate and product states of isomerization reactions

In order to avoid problems with non-ergodic sampling due to the presence of significant barriers separating individual stable rotamers in a given intermediate state of interest (X = R, I_2, I_3), probability density of a reference state ($\xi_{ref,X}$) has been determined as a product of two terms ($P(\xi_{ref,X}) = \tilde{P}(\xi_{ref,X})\, p(X(I))$), each being computed separately as discussed in Section 3.2. In this section we provide the probability densities $\tilde{P}(\xi_{ref,X})$. The reference state $\xi_{ref,X}$ was chosen so as to achieve a sufficiently high probability density, so that $\tilde{P}(\xi_{ref,X})$ could be determined with a good accuracy in a MD run. According to Equations (1) and (2) presented in the main text, the results of free energy calculation are independent of the choice of the reference state, provided the value of $\tilde{P}(\xi_{ref,X})$ is determined accurately. In Section SIV.1, we provide probability densities $\tilde{P}(\xi_{ref,R})$ for the reactant of mechanisms I and II. Straightforward molecular dynamics has been used for these calculations. In Sections SIV.2 and SIV.3, $\tilde{P}(\xi_{ref,X})$ are computed for the relevant mixture of rotational isomers of I_2 and I_3 by determination of a weighted histogram using the configurations sampled in the blue moon sampling of the torsion coordinate performed for the states I_2 and I_3 (see Section SII). The values of $P(\xi_{ref,X})$ computed with $p(X(I))$ are also reported (Equation 5 in the main text).

SIV.1. Reactant R

Figure S7 and Figure S8 show the distributions $\tilde{P}(\xi_{ref,R})$ for different rotamers of the species R, determined for different approximations to reaction coordinate used to study mechanisms I and II. The numerical values of the corresponding reference states are collected in Table S4. As the barriers separating different rotamers of R are large enough to effectively prevent mutual interconversions within our relatively short MD runs, we were able to sample the R(I) and R(II) rotational isomers separately in straightforward molecular dynamics.

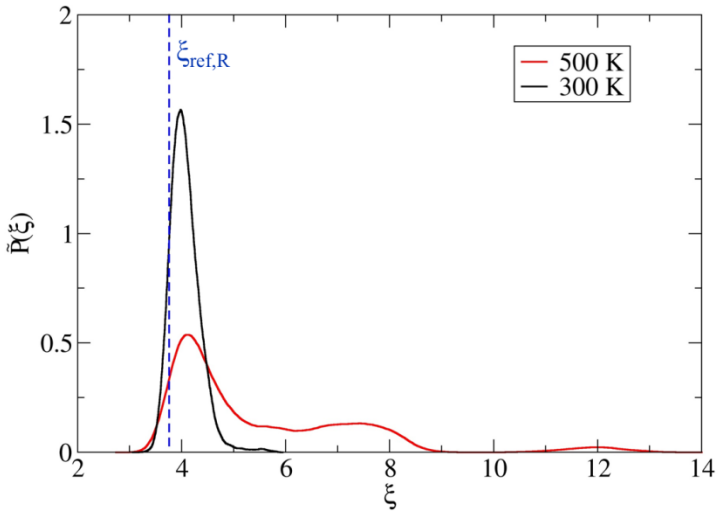

Figure S7. Probability distribution functions $\tilde{P}(\xi)$ computed for the reactant state R(I) at 300 K and 500 K.

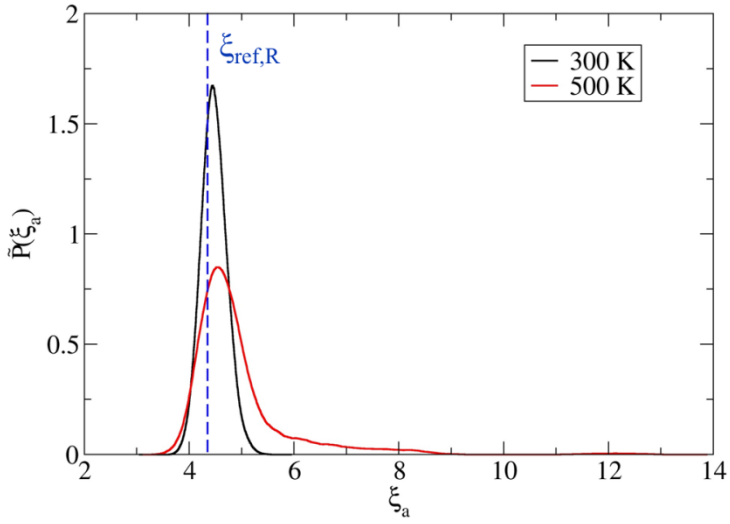

Figure S8. Probability distribution functions $\tilde{P}(\xi)$ computed for the reactant state R(II) at 300 K and 500 K.

Table S4. Values of ξ_{ref} for the reactant states R(I) and R(II), and the corresponding values of the probability density ($\tilde{P}(\xi_{ref,R})$). The lengths of production runs of MD simulations (τ) used to compute $\tilde{P}(\xi_{ref,R})$ are also listed. Note that the values of ξ_{ref} and $\tilde{P}(\xi_{ref,R})$ listed for the reactant of mechanisms I and II differ because of the use of different approximations to reaction coordinate.

	Mechanism I				
	T (K)	τ (ps)	$\xi_{ref,R}$	$\tilde{P}(\xi_{ref,R})$	P$(\xi_{ref,R})$
Reactant R(I)	300	100	3.76	0.94	0.055
	500	200	3.76	0.34	0.057

	Mechanism II				
	T (K)	τ (ps)	$\xi_{ref,R}$	$\tilde{P}(\xi_{ref,R})$	P$(\xi_{ref,R})$
Reactant R(II)	300	180	4.35	1.51	0.84
	500	180	4.35	0.74	0.37

SIV.2. Intermediate I_2

The first reaction step of mechanism II does not require formation of a specific rotamer for I_2 and, consequently, the rotational isomers (I) and (III) (see Section SI.1) have been formed in the constrained MD simulations of I_2. Importantly, swapping between these two states has no significant effect on the value of free energy gradient indicating that the corresponding transformation between the rotamers is decoupled from the approximation to the reaction coordinate used in our calculations. In these constrained MD simulations, the states I_2(I) and I_2(III) are present at similar proportions as those deduced from the free energy profile shown in Figure S3.

In order to determine the value of $\tilde{P}(\xi_{ref,I_2})$, we used the data from the constrained MD simulations employed in calculations of the free energy profiles described in Section SII.1, taking into account the symmetry equivalent atoms in the analysis of the approximation to reaction coordinate:

$$\tilde{P}(\xi_{ref,I_2}) = \frac{\int_{I_2(I),I_2(III)} d\tau\ \delta(\xi - \xi_{ref,I_2}) \exp\left\{-\frac{A(\tau)}{k_B T}\right\}}{\int_{I_2(I),I_2(III)} d\tau\ \exp\left\{-\frac{A(\tau)}{k_B T}\right\}}, \qquad \text{(Eq. S3)}$$

the probability density of the reference being defined by:

$$P(\xi_{ref,I_2}) = \tilde{P}(\xi_{ref,I_2})\ p(I_2(I), I_2(III)), \qquad \text{(Eq. S4)}$$

with:

$$p(I_2(I), I_2(III)) = \frac{\int_{I_2(I),I_2(III)} d\tau \exp\left\{-\frac{A(\tau)}{k_B T}\right\}}{\int_{I_2} d\tau \exp\left\{-\frac{A(\tau)}{k_B T}\right\}}. \qquad \text{(Eq. S5)}$$

The resulting probability distribution functions $\tilde{P}(\xi)$ are displayed in Figure S9 and the relevant numerical values are compiled in Table S5 along with $P\left(\xi_{ref,I_2}\right)$.

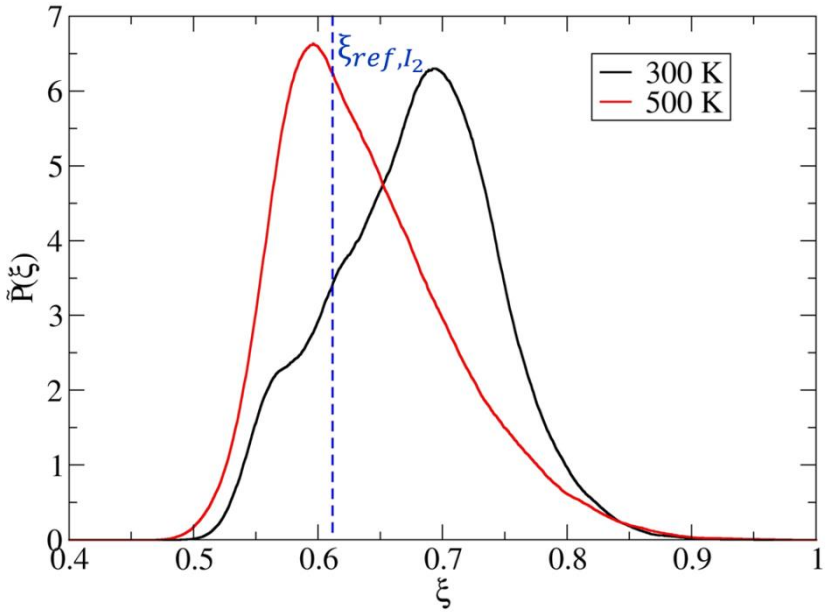

Figure S9. Probability distribution functions $\tilde{P}(\xi)$ computed for the intermediate state I_2 formed in the first step of mechanism II at 300 K and 500 K.

The second reaction step of mechanism II is a type B isomerization and it requires a specific arrangement of the state I_2 that corresponds to the rotational isomer I_2(II). The values of $\tilde{P}\left(\xi_{ref,I_2}\right)$ were obtained in a similar procedure as described above for the first reaction step whereby the data from our constrained MD runs with controlled value of τ have been employed. The resulting probability distribution functions $\tilde{P}(\xi)$ are given in Figure S10 and the numerical results are compiled in Table S5 along with $P\left(\xi_{ref,I_2}\right)$.

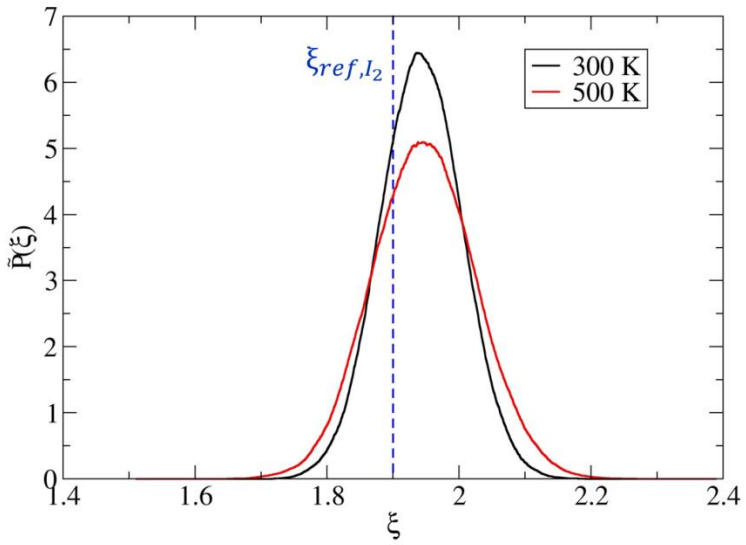

Figure S10. Probability distribution function $\tilde{P}(\xi\ )$ computed for the intermediate state I_2 considered as reactant in the second step of mechanism II at 300 K and 500 K.

Table S5. Values of ξ_{ref} for the intermediate I_2 playing role of the product state for mechanism II, step 1, and reactant state of mechanism II, step 1, and the corresponding values of probability densities $\tilde{P}(\xi_{ref,I_2})$ and $P(\xi_{ref,I_2})$. Note that the values of ξ_{ref,I_2} and $\tilde{P}(\xi_{ref,I_2})$ listed for the two reaction steps differ because of the use of different approximation to reaction coordinate.

	Mechanism II, step 1			
	T (K)	ξ_{ref,I_2}	$\tilde{P}(\xi_{ref,I_2})$	$P(\xi_{ref,I_2})$
Intermediate I_2	300	0.61	3.41	2.38
	500	0.61	6.23	4.87

	Mechanism II, step 2			
	T (K)	ξ_{ref,I_2}	$\tilde{P}(\xi_{ref,I_2})$	$P(\xi_{ref,I_2})$
Intermediate I_2	300	1.90	5.12	1.54
	500	1.90	4.28	0.93

SIV.3. Product I_3

Mechanism I

At 300 K, both the rotamers I_3(I) and I_3(II), separated by a small barrier (see Section S1.2), are formed in our blue moon simulations. Similarly, I_3(III) and I_3(IV) are present at 500 K. The resulting probability distribution functions $\tilde{P}(\xi)$ are computed using our constrained MD data (see Section SII.2) for these particular blends of rotamers as in Section SIV.2 and they are given in Figure S11 and the corresponding numerical results are compiled in Table S6.

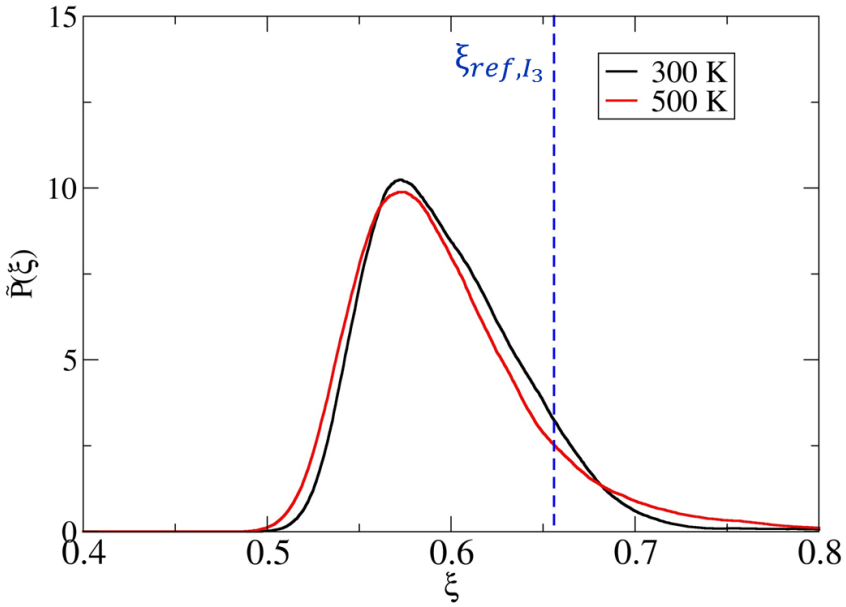

Figure S11. Probability distribution function $\tilde{P}(\xi)$ computed for the product I_3 formed via mechanism I at 300 K and 500 K.

Mechanism II

As a product of type B isomerization reaction (second step of Mechanism II), the specific rotational isomer I_3(III) is formed, hence we determined the value of $\tilde{P}(\xi_{ref,I_3})$ for this specific rotamer. Once again, our constrained MD data from the free energy calculations presented in Section SII.2 were employed for this purpose and the resulting probability distribution functions $\tilde{P}(\xi)$ are given in Figure S12 while the corresponding numerical results are compiled in Table S6.

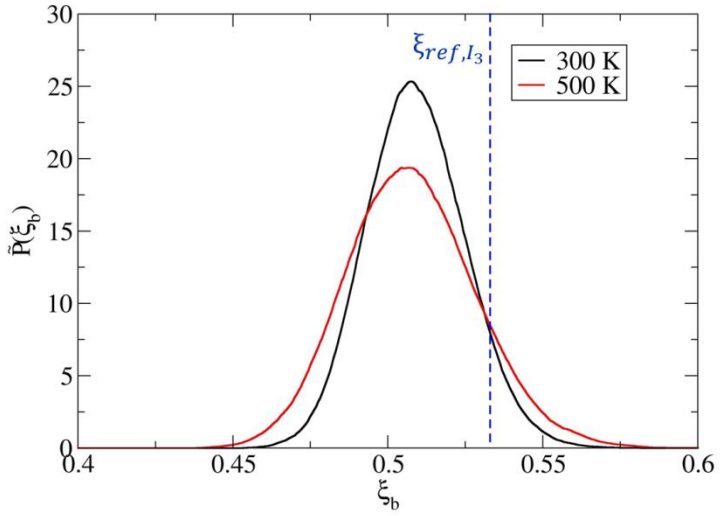

Figure S12**.** Probability distribution function $\tilde{P}(\xi)$ computed for the product I_3(III) of mechanism II at 300 K and 500 K.

Table S6. Values of ξ_{ref} for the product I_3 of mechanisms I and II, and the corresponding values of probability density ($\tilde{P}(\xi_{ref,I_3})$). The values of ξ_{ref} and $\tilde{P}(\xi_{ref,I_3})$ listed for the mechanisms I and II are different because of the use of different approximation to reaction coordinate.

	Mechanism I			
	T (K)	ξ_{ref,I_3}	$\tilde{P}(\xi_{ref,I_3})$	$P(\xi_{ref,I_3})$
Product I_3	300	0.66	3.0	2.39
	500	0.66	2.5	1.08

	Mechanism II			
	T (K)	ξ_{ref,I_3}	$\tilde{P}(\xi_{ref,I_3})$	$P(\xi_{ref,I_3})$
Product I_3	300	0.53	7.85	0.44
	500	0.53	8.42	1.46

SV. Avoiding the by-reactions

In our free energy calculations, several undesired by-reactions could occur. For instance, the cations (mainly the secondary ones) can undergo occasional deprotonations or alkoxide formations. In order to restrict the sampling to the part of configurational space of interest, we followed the same strategy as in our previous work.[5] A restraining potential of the following form

$$V(R) = \frac{1}{2}K(R - R_0)^2 \qquad \text{(Eq. S6)}$$

has been added to reinforce the 13 C-H bonds involving hydrogen atoms which are not directly involved in the reactions of interest (*i.e.* all CH bonds except those involving H^1 and H^2, see Figure 5 in the main text). In Equation S6, R stands for the interatomic bonding distance C-H, R_0 =1.1 Å corresponds to an approximate equilibrium length of the C-H bond, and the force constant K is set to 100 eV.Å^{-2}.

We had to prevent also other by-reactions such as the formation of an alkoxide formation between the C^2 atom of the secondary cation I_1 and the oxygen atom O^1 of the zeolitic framework, and the formation of a pi-complex by deprotonation of the newly formed I_1 (when H^1 returns to the framework oxygen atom next to the aluminium atom in Figure 5). A smeared step potential (shown in Figure S13) acting on the distance R between the corresponding atoms was used to prevent these processes:

$$V(R) = \frac{A_i}{1 + exp\left(-D\left(\frac{\mathrm{R}}{\mathrm{R}_{0,i}} - 1\right)\right)}, \qquad \text{(Eq. S7)}$$

where the parameters were set to the following values: $A = -2$ eV, $D = 20$, $\mathrm{R}_{0,i} = 2.5$ Å for CO and $\mathrm{R}_{0,i} = 1.5$ Å for OH. The restraining potential shown in Figure S13 generates extra forces acting on atoms only if a fluctuation attempts to create the C-O or O-H bonds involved.

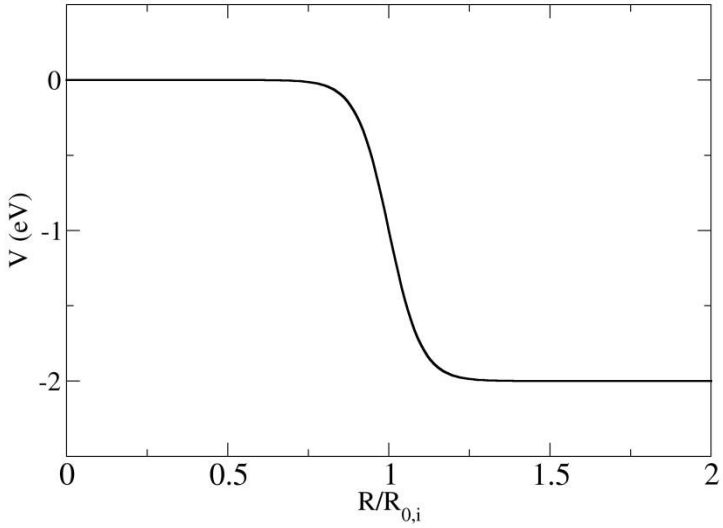

Figure S13**.** Restraining smeared step potential acting on a distance *R* between two atoms.

Yet another undesired processes that could occur in the case of the isomerization reactions are the transformations of rotational isomers into one another. As explained in Section 3.1, it is crucial to control the presence of appropriate rotamer in the blue moon sampling simulation of the reactant R because the mechanism under consideration depends on the arrangement of reactant. For the reactant R, the free energy barriers between rotamers are large enough (see Figure 3 in the main text) to prevent frequent transformations. We checked the value of the dihedral angle (τ) between the atoms C^2, C^3, C^4, and C^7 characterizing the rotamers and we restarted the simulations in rare cases where an undesired transformation between rotamers occurred.

The second step of mechanism II also requires formation of a specific rotational isomer of the cations I_2 and I_3. In particular, the hydrogen atom H^2 must be in position sterically favorable for its shift from C^2 to C^3.

In the constrained simulations of I_2 at 300 K, only the rotamer I_2(II) was observed (see Section SII.1). At 500 K, the rearrangements between different rotamers were frequent for the two points of the blue moon simulation near I_2 and we used a smeared step restraining potential acting on the dihedral angle (τ) defined by the atoms C^1, C^2, C^3 and C^4. This restraining potential is shown in Figure S14 and its form is as follows:

$$V(\tau) = \sum_{i=1}^{2} \frac{A_i}{1 + exp\left(-D_i\left(\frac{\tau}{\tau_{0,i}} - 1\right)\right)}, \qquad \text{(Eq. S8)}$$

where the parameters were set to the following values: $A_1 = 2$ eV, $D_1 = 100$, $\tau_{0,1} = -115°$, and $A_2 = -2$ eV, $D_2 = 20$, $\tau_{0,2} = -11°$.

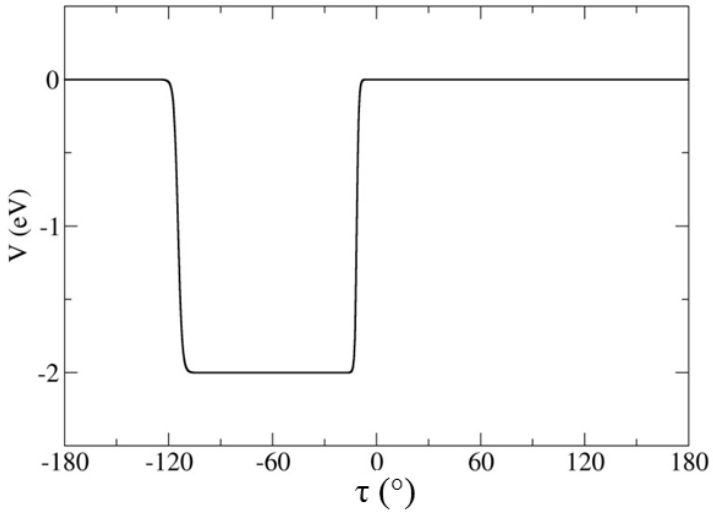

Figure S14. Restraining potential acting on the dihedral angle C^3-C^2-C^4-C^5 (θ).

Once again, the restraining potential is flat in the region defining the rotamer I_2(II) (–115° < τ < –11°) and hence the forces due to $V(\tau)$ are negligible unless a transition to some other rotamer is attempted. This assumption was demonstrated by reproducing the constrained simulation on the third point of the simulation, where only I_2(II) was present. The same value for the gradient of the free energy was obtained with and without the restraining potential acting on τ, confirming the correct convergence of the gradient and a negligible effect of the restraining potential.

SVI. Kinetic analysis

In order to compare relative importance of two competing reaction mechanisms I and II of transformation of reactant state R into product I_3, a simple kinetic model has been used in which two processes involving common initial and final states have been considered:

$$R \rightleftharpoons I_3, \qquad \text{(Eq. S9)}$$

$$R \rightleftharpoons I_2 \rightleftharpoons I_3. \qquad \text{(Eq. S10)}$$

The corresponding kinetic equations

$$\frac{dc_R(t)}{dt} = -\left(k_{R\to I_3} + k_{R\to I_2}\right)c_R(t) + k_{I_2\to R}c_{I_2}(t) + k_{I_3\to R}c_{I_3}(t), \qquad \text{(Eq. S11)}$$

$$\frac{dc_{I_2}(t)}{dt} = k_{R\to I_2}c_R(t) + k_{I_3\to I_2}c_{I_3}(t) - \left(k_{I_2\to R} + k_{I_2\to I_3}\right)c_{I_2}(t), \qquad \text{(Eq. S12)}$$

$$c_R(t) + c_{I_2}(t) + c_{I_3}(t) = c_R(0) \qquad \text{(Eq. S13)}$$

have been solved using a simple Euler method with time steps of 10^{-5} s and 10^{-12} s for T=300 K and 500 K, respectively. The following initial concentrations have been considered: $c_R(0) = 1$ mol/m^3, $c_{I_2}(0) = c_{I_3}(0) = 0$ mol/m^3. The rate constants k_X for the process X have been computed using the Eyring equation. The rate constants $k_{I_3\to R}$ and $k_{I_3\to I_2}$ have been computed using the average value of free energies of the state I_3 computed for the mechanisms I and II. The integration was stopped after the period T when the condition $c_{I_3}(t = T) = 0.10 \cdot c_R(0)$ was fulfilled or when equilibrium was established (whatever came first). Such a low conversion regime corresponds to reaction conditions at which the reverse reactions from the final state I_3 can be neglected. The percentage of the product molecules formed via mechanism I was determined as

$$x_I = \frac{\int_0^T dt\, k_{R\to I_3}c_R(t)}{\int_0^T dt\, k_{R\to I_3}c_R(t) + \int_0^T dt\, k_{I_2\to I_3}c_{I_2}(t)} \times 100\% \qquad \text{(Eq. S14)}$$

and the same quantity for the mechanism II is defined as $x_{II} = 100\% - x_I$. In order to explore the effect of the statistical uncertainty on the values of x_I and x_{II}, 2000 independent evaluations of the kinetic model have been performed, whereby the free energy barriers have been modified by adding a noise uniformly distributed within ± 5 kJ/mol intervals (except of the steps $I_3 \to R$ and $I_3 \to I_2$ for which the noise was distributed over wider interval of ± 9 kJ/mol chosen to reflect large uncertainty in computed free energy of the state I_3). The standard deviation of mean values computed in such a way provide us with an estimate of error (i.e. standard error) for the quantities x_I and x_{II}. The values for x_I (x_{II}) determined for T=300 K and 500 K are, respectively, 21.0 $\pm$ 1.6 % and 75.4 $\pm$ 1.4 % (79.0 $\pm$ 1.6 % and 24.6 $\pm$ 1.4 %). Note that, as expected for the low coverage regime employed here, very similar results (x_I of 25.5 $\pm$ 0.2 % at 300 K and 72.5 $\pm$ 0.2 % at 500 K) were obtained with a simplified model completely neglecting the reverse reactions from the final state I_3 that are most significantly affected by the statistical errors of free energies of activation (see Section 4.1. in the main text).

SVII. Static calculations for the gas phase reactions

In this section we provide thermodynamic data for the two mechanisms in gas phase computed using the harmonic transition state theory[6] within the static approach, along with the rigid rotor and ideal gas approximations: individual contributions of different types of degrees of freedom to free energies of activation $\Delta A_{X_i(j)\to TS_i}$ and to free energies of reaction $\Delta A_{X_i(j)\to Y_i(k)}$ for the microprocess transformation starting from the active rotamer $X_i(j)$ of the reactant X_i and yielding the rotamer $Y_i(k)$ of the product Y_i.

Table S7. Electronic free energies A_{el} for the molecules in the gas phase. All values are in kJ/mol.

	Mechanism I		
	I_1(I)	TS(I)	I_3(I)
A_{el}	-10942.14	-10926.98	-11004.68

	Mechanism II, step 1		
	I_1(II)	TS(IIa)	I_2(III)
A_{el}	-10955.62	-10953.33	-11000.93

	Mechanism II, step 2		
	I_2(II)	TS(IIb)	I_3(III)
A_{el}	-10998.25	-10918.24	-10998.54

Table S8**.** Individual contributions to the $\Delta A_{I_1(I)\rightarrow TS(I)}$ and $\Delta A_{I_1(I)\rightarrow I_3(I)}$ terms computed for mechanism I of the reaction in the gas phase. All values are in kJ/mol.

	T=300 K		T=500 K	
	$I_1(I) \rightarrow TS(I)$	$I_1(I) \rightarrow I_3(I)$	$I_1(I) \rightarrow TS(I)$	$I_1(I) \rightarrow I_3(I)$
ΔA_{el}	15.2	-62.5	15.2	-62.5
ΔA_{vib}	6.7	0.5	12.4	1.1
ΔA_{rot}	0.2	0.1	0.4	0.1
ΔA_{trans}	0.0	0.0	0.0	0.0
$\boldsymbol{\Delta A_{total}}$	**22.0**	**-62.0**	**27.9**	**-61.3**
ΔU_{el}	15.2	-62.5	15.2	-62.5
ΔU_{vib}	-1.0	-0.6	-3.2	-0.4
ΔU_{rot}	0.0	0.0	0.0	0.0
ΔU_{trans}	0.0	0.0	0.0	0.0
$\boldsymbol{\Delta U_{total}}$	**14.1**	**-63.1**	**12.0**	**-63.0**
$T\Delta S_{el}$	0.0	0.0	0.0	0.0
$T\Delta S_{vib}$	-7.7	-1.0	-15.6	-1.6
$T\Delta S_{rot}$	-0.2	-0.1	-0.4	-0.1
$T\Delta S_{trans}$	0.0	0.0	0.0	0.0
$\boldsymbol{T\Delta S_{total}}$	**-7.9**	**-1.1**	**-16.0**	**-1.7**

Table S9. Individual contributions to the $\Delta A_{I_1(II)\rightarrow TS(IIa)}$ and $\Delta A_{I_1(II)\rightarrow I_2(I)}$ terms computed for the first step of mechanism II of the reaction in the gas phase. All values are in kJ/mol.

	T=300 K		T=500 K	
	$I_1(II) \rightarrow TS(IIa)$	$I_1(II) \rightarrow I_2(I)$	$I_1(II) \rightarrow TS(IIa)$	$I_1(II) \rightarrow I_2(I)$
ΔA_{el}	2.3	-45.3	2.3	-45.3
ΔA_{vib}	-0.3	-7.3	2.9	-10.4
ΔA_{rot}	0.1	0.0	0.2	0.0
ΔA_{trans}	0.0	0.0	0.0	0.0
$\boldsymbol{\Delta A_{total}}$	**2.1**	**-52.6**	**5.4**	**-55.7**
ΔU_{el}	2.3	-45.3	2.3	-45.3
ΔU_{vib}	-4.5	-2.7	-6.2	-2.5
ΔU_{rot}	0.0	0.0	0.0	0.0
ΔU_{trans}	0.0	0.0	0.0	0.0
$\boldsymbol{\Delta U_{total}}$	**-2.2**	**-48.0**	**-3.9**	**-47.8**
$T\Delta S_{el}$	0.0	0.0	0.0	0.0
$T\Delta S_{vib}$	-4.2	4.6	-9.1	8.0
$T\Delta S_{rot}$	-0.1	0.0	-0.2	0.0
$T\Delta S_{trans}$	0.0	0.0	0.0	0.0
$\boldsymbol{T\Delta S_{total}}$	**-4.3**	**4.6**	**-9.2**	**8.0**

Table S10. Individual contributions to the $\Delta A_{I_2(II)\rightarrow TS(IIb)}$ and $\Delta A_{I_2(II)\rightarrow I_3(III)}$ terms computed for the second step of mechanism II of the reaction in the gas phase. All values are in kJ/mol.

	T=300 K		T=500 K	
	$I_2(II) \rightarrow TS(IIb)$	$I_2(II) \rightarrow I_3(III)$	$I_2(II) \rightarrow TS(IIb)$	$I_2(II) \rightarrow I_3(III)$
ΔA_{el}	80.0	-0.3	80.0	-0.3
ΔA_{vib}	4.0	0.7	9.3	0.3
ΔA_{rot}	0.4	0.2	0.6	0.4
ΔA_{trans}	0.0	0.0	0.0	0.0
$\boldsymbol{\Delta A_{total}}$	**84.4**	**0.6**	**89.9**	**0.4**
ΔU_{el}	80.0	-0.3	80.0	-0.3
ΔU_{vib}	-3.1	1.1	-4.8	1.3
ΔU_{rot}	0.0	0.0	0.0	0.0
ΔU_{trans}	0.0	0.0	0.0	0.0
$\boldsymbol{\Delta U_{total}}$	**76.9**	**0.8**	**75.2**	**1.1**
$T\Delta S_{el}$	0.0	0.0	0.0	0.0
$T\Delta S_{vib}$	-7.1	0.4	-14.1	1.0
$T\Delta S_{rot}$	-0.4	-0.2	-0.6	-0.4
$T\Delta S_{trans}$	0.0	0.0	0.0	0.0
$\boldsymbol{T\Delta S_{total}}$	**-7.5**	**0.2**	**-14.7**	**0.6**

SVIII. Structural data

SVIII.1. Analysis of the C-C bonds involved in the PCPs

The probability distribution functions for the three C-C bonds (C^2-C^3, C^3-C^4 and C^2-C^4) involved in the PCP of the transition states determined using the data generated by MD are shown in Figure 9 in the main text. These distributions were fitted by the Gaussian function:

$$f(d) = \frac{1}{\sqrt{2\pi\sigma^2}} exp\left(-\frac{(d-\mu)^2}{2\sigma^2}\right). \qquad \text{(Eq. S15)}$$

Assuming that each bond (d) can be represented by a harmonic oscillator with the force constant κ, the standard deviation (σ) of the corresponding distribution can be identified[7] with the term $\sqrt{\frac{k_B T}{\kappa}}$. Hence the relative strength of the bond can be estimated from the width of the corresponding probability distribution. The parameter μ stands for the average length of the bond. The values of the fitting parameters μ and σ are presented in Table S11.

Table S11. Parameters μ and σ (in Å) obtained by fitting of the MD data for the three edge protonated cyclopropanes obtained as transition states of mechanism (I) (TS(I)), mechanism II, step 1 (TS(IIa)) and mechanism II, step 2 (TS(IIb)).

TS(I)

T = 300K	μ	σ
C^2-C^3	1.434	0.035
C^3-C^4	1.808	0.054
C^2-C^4	1.623	0.067

T = 500K	μ	σ
C^2-C^3	1.445	0.043
C^3-C^4	1.802	0.069
C^2-C^4	1.620	0.076

TS(IIa)

T = 300K	μ	σ
C^2-C^3	1.472	0.041
C^3-C^4	1.548	0.040
C^2-C^4	1.890	0.055

T = 500K	μ	σ
C^2-C^3	1.456	0.039
C^3-C^4	1.576	0.054
C^2-C^4	1.918	0.076

TS(IIb)

T = 300K	μ	σ
C^2-C^3	1.757	0.049
C^3-C^4	1.468	0.031
C^2-C^4	1.576	0.044

T = 500K	μ	σ
C^2-C^3	1.757	0.062
C^3-C^4	1.473	0.042
C^2-C^4	1.580	0.058

SVIII.2. Secondary cation

In mechanism I, the structures for the rotamer I_1(I) of the secondary cation have been identified with the point ξ = 2.15 of the simulation, corresponding to the local free energy minimum occurring at 500 K (Figure 6). Similarly, in mechanism II, for the rotamer I_1(II), we identified the secondary cation with the point ξ = 2.15 of the blue moon simulation which is a very shallow

minimum at 500 K (Figure 7). The probability distribution functions for the C-C bonds (C^2-C^3, C^3-C^4 and C^2-C^4) of the rotamer I_1(I) and I_1(II) of the secondary cation determined using the data generated by MD are shown Figure S15.

We note that the probability distribution functions of C^2-C^4 and C^2-H^2 distances are sensitive to temperature and openings of the $C^2C^3C^4$ triangle occur when the temperature increases. This effect is more important for I_1(II).

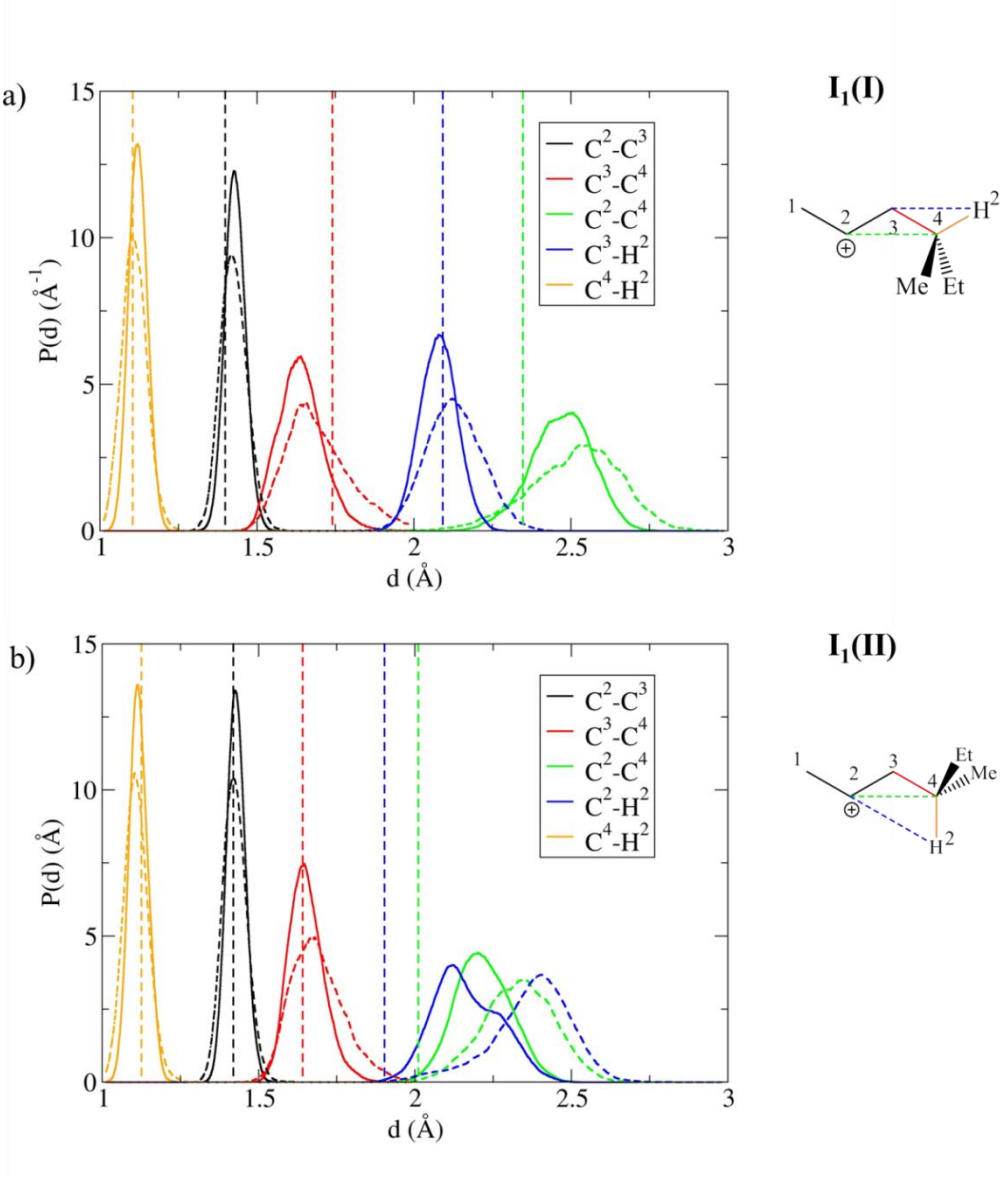

Figure S15. Probability distribution functions of selected C-C and C-H bonds in the two reactive rotamers of the secondary carbenium ion I_1 in (a) I_1(I), and (b) I_1(II) determined using MD at 300K (solid lines) and 500K (dash lines). The static approach results for the gas phase reaction are reported by vertical dashed lines.

SVIII.3. Transition state of protonation

The probability distribution functions for the O^1-H^1 distance and C^1-H^1 distance in the transition state of protonation of the initial alkene R(I) are shown in Figure S16. In the case of mechanism I at T=500 K, this transition state is located at $\xi^* = 2.76$ (Figure 6 in the main text).

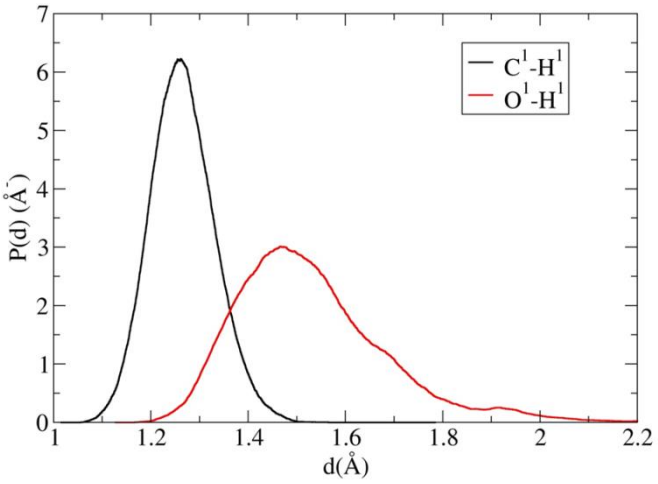

Figure S16. Probability distributions of C^1-H^1 and O^1-H^1 distances in the transition state of protonation occurring in mechanism I at 500 K.

SIX. Interaction of alkene in the reactant state with the acid site of the zeolite

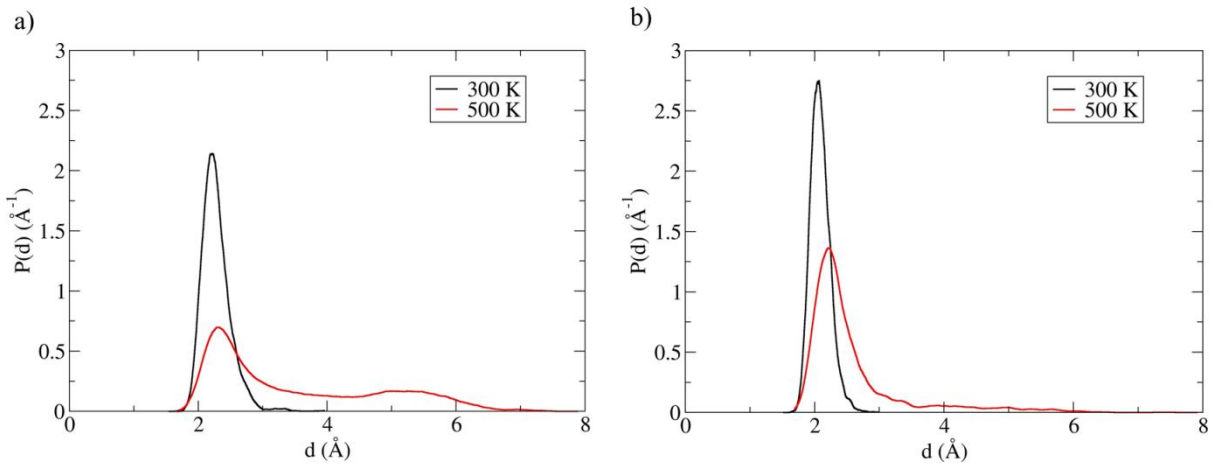

Figure S17. Distance d between the hydrogen atom of the zeolite and the center of the C=C bond in the free MD runs of reactant a) R(I) and b) R(II).

As shown in Figure S15, the adsorption complex formed by the alkene in the reactant configuration and the acid site of zeolite is fairly stable at both temperatures considered in this work: the distributions $P(d)$ are peaked at ~2.1 Å and the molecule spends the majority of simulation time (99% at 300 K and 51 % at 500 K) in the vicinity of the acid site with d<3.0 Å.

SX. Statistical Error Estimations

Using standard formulae for error propagation[8], the standard error for the free energy of activation ($\sigma(\Delta A^{\ddagger})$) computed using Equation (1) writes:

$$\sigma(\Delta A^{\ddagger}) = \sqrt{\sigma^2(\Delta A_{\xi_{ref,X}\to\xi^*}) + (k_B T)^2 \sigma^2\left(\ln\left(\frac{h}{k_B T}\frac{\langle|\dot{\xi}^*|\rangle}{2}P(\xi_{ref,X})\right)\right)}. \qquad \text{(Eq. S16)}$$

According to our tests, the most significant contributions to $\sigma(\Delta A^{\ddagger})$ are from the terms $\sigma(\Delta A_{\xi_{ref,X}\to\xi^*})$ while the uncertainties from the terms $\langle|\dot{\xi}^*|\rangle$ and $\sigma\left(\ln\left(P(\xi_{ref,X})\right)\right)$ turned out to be small compared to the dominant sources of statistical error and were neglected in this work, simplifying thus the expression for $\sigma(\Delta A^{\ddagger})$ to

$$\sigma(\Delta A^{\ddagger}) = \sqrt{\sigma^2(\Delta A_{\xi_{ref,X} \to \xi^*})}. \quad \text{(Eq. S17)}$$

An analogous formula:

$$\sigma(\Delta A_{X \to Y}) = \sqrt{\sigma^2\left(\Delta A_{\xi_{ref,X} \to \xi_{ref,Y}}\right)}. \quad \text{(Eq. S18)}$$

was used to estimate the statistical uncertainty for the free energies of reaction.

As the term $\Delta A_{\xi_{ref,X} \to \xi^*}$ is computed via numerical integration using the expression

$$\Delta A_{\xi_{ref,X} \to \xi^*} = \sum_{i=1}^{M} w_i A_i',$$

where the sum is over all integration points, w_i is the weight whose value depends on the choice of the integration algorithm (here $w_i = \frac{\xi_{i+1} - \xi_i}{2}$ for $i = 1$ and $i = M$, and $w_i = \frac{\xi_{i+1} - \xi_{i-1}}{2}$ for $1 < i < M$) and A_i' is the free energy gradient evaluated at the point ξ_i. The corresponding standard error $\sigma(\Delta A_{\xi_{ref,X} \to \xi^*})$ therefore writes

$$\sigma\left(\Delta A_{\xi_{ref,X} \to \xi^*}\right) = \sqrt{\sum_{i=1}^{M} w_i^2 \sigma^2(A_i')}, \quad \text{(Eq. S19)}$$

where the terms $\sigma(A_i')$ are determined using the block method of Flyvbjerg and Petersen.[9,10] The error bars reported in this work correspond to confidence interval of 95 %, i.e. the uncertainty in the computed free energies of activation and of reaction are expressed as $\pm 1.96 \cdot \sigma(\Delta A^{\ddagger})$ and $\pm 1.96 \cdot \sigma(\Delta A_{X \to Y})$, respectively.

SXI. Variation of selected geometric parameters along the reaction coordinate for the different mechanisms

Selected geometric parameters have been monitored in our blue moon simulations of both mechanisms at 300 K and 500 K. The different evolutions are consistent with the chemical processes described.

For mechanism I, the average values are shown in Figure S18. As expected, the variation of geometric parameters follows the same trend at both temperatures. Note that the large fluctuation in the distance O^1-H^1 observed for $\xi < 3.5$ (i.e. where H has been transferred to the hydrocarbon) is caused by rotations and translations of cation in the zeolite.

For mechanism II, step 1, the average values are shown in Figure S19. As for mechanism I, large fluctuations of O^1-H^1 distance occur for $\xi < 2.0$ where H has been transferred to the hydrocarbon. The average values for mechanism II, step 2 are shown in Figure S20.

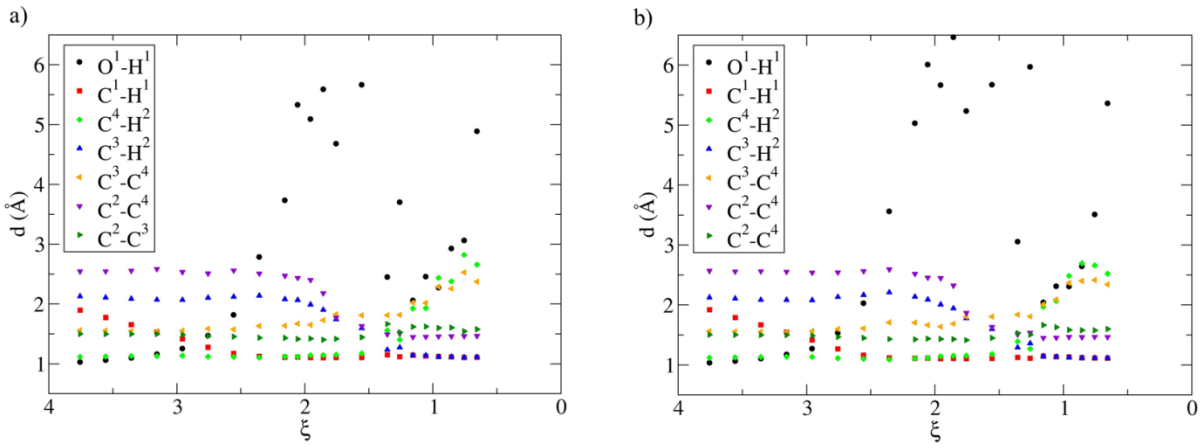

Figure S18. Evolution of selected distances along the reaction coordinates for mechanism I. a) T=300 K and b) T=500 K.

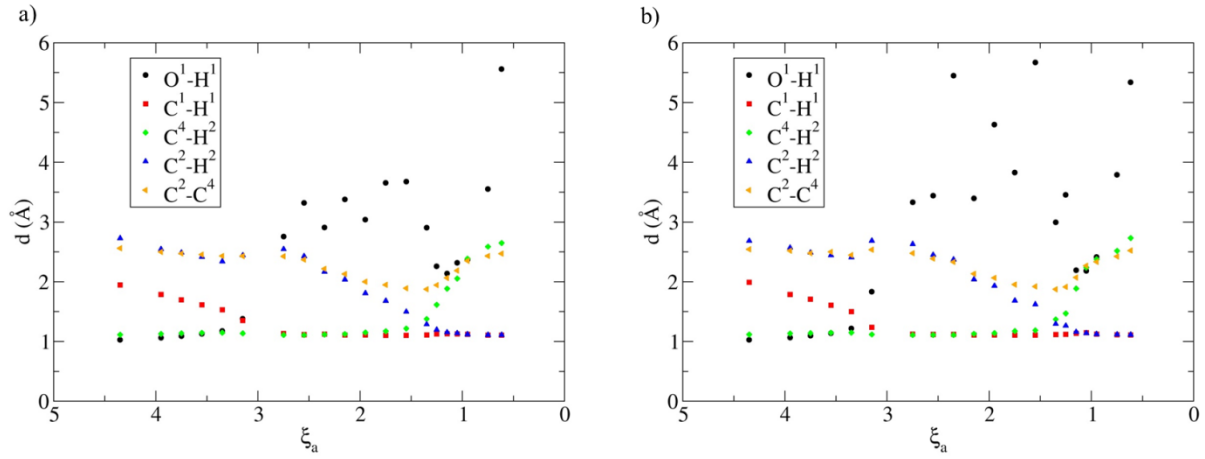

Figure S19. Evolution of selected distances along the reaction coordinates for mechanism II, step 1. a) T=300 K and b) T=500 K.

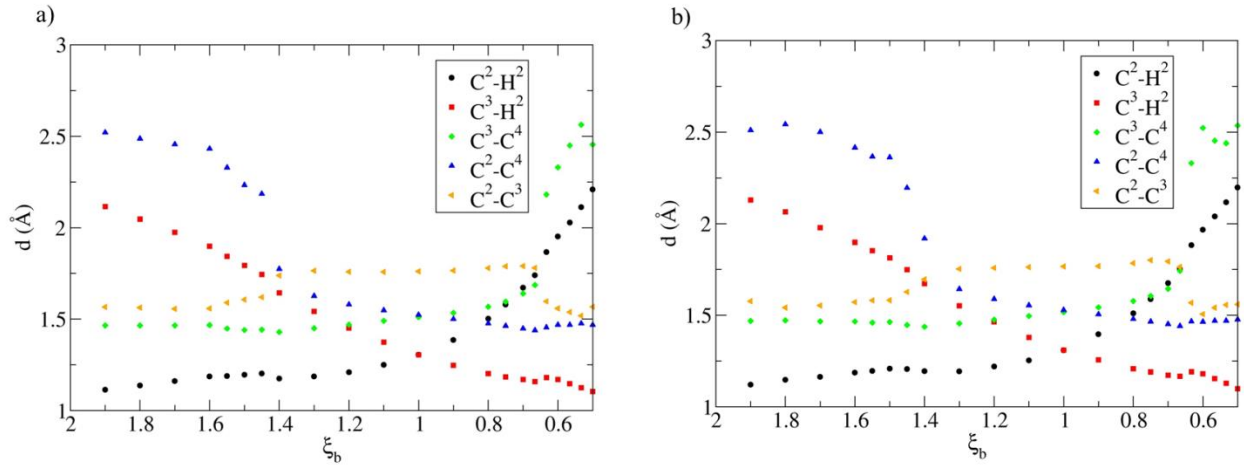

Figure S20. Evolution of selected distances along the reaction coordinates for mechanism II, step 2. a) T=300 K and b) T=500 K.

References

(1) Baerlocher, C., McCusker, J. K. International Zeolite Association. http://www.iza-structure.org/databases/.

(2) Smith, L. J.; Davidson, A.; Cheetham, A. K. A Neutron Diffraction and Infrared Spectroscopy Study of the Acid Form of the Aluminosilicate Zeolite, Chabazite (H- SSZ-13). *Catal. Lett.* **1997**, *49*, 143–146.

(3) Carter, E. A.; Ciccotti, G.; Hynes, J. T.; Kapral, R. Constrained Reaction Coordinate Dynamics for the Simulation of Rare Events. *Chem. Phys. Lett.* **1989**, *156*, 472–477.

(4) Henriksen, N. E.; Hansen, F. Y. *Theories of Molecular Reaction Dynamics: The Microscopic Foundation of Chemical Kinetics;* Oxford University Press, 2008.

(5) Rey, J.; Gomez, A.; Raybaud, P.; Chizallet, C.; Bučko, T. On the Origin of the Difference Between Type A and Type B Skeletal Isomerization of Alkenes Catalyzed by Zeolites: The Crucial Input of ab initio Molecular Dynamics. *J. Catal.* **2019**, *373*, 361–373.

(6) Eyring, H. The Activated Complex in Chemical Reactions. *J. Chem. Phys.* **1935**, *3*, 107–115.

(7) Baron, R.; van Gunsteren, W. F.; Hünenberger, P. H. Estimating the Configurational Entropy from Molecular Dynamics Simulations: Anharmonicity and Correlation Corrections to the Quasi-Harmonic Approximation. *Trends Phys. Chem.* **2006**, *11*, 87–122.

(8) Ku, H. H. Notes on the Use of Propagation of Error Formulas. *J. Res. Nat. Bur. Stand., Sec. C* **1966**, *70C*, 263–273.

(9) Flyvbjerg, H.; Petersen, H. G. Error Estimates on Averages of Correlated Data. *J. Chem. Phys.* **1989**, *91*, 461–466.

(10) Frenkel, D.; Smit, B. *Understanding Molecular Simulation*. *From Algorithms to Applications*; Computational science series; Academic Press, 2002.